Airborne GNSS reflectometry for coastal monitoring of sea state

Monitoreo del estado del mar en zonas costeras usando GNSS reflectometría

Mario Moreno[1]

Abstract

Sea level rise and sea state variability, resulting from climate change and global warming, are critical research areas. However, current techniques for observing and monitoring these phenomena have limitations in terms of spatial and temporal resolution, particularly in dynamic coastal zones. GNSS Reflectometry (GNSS-R) is an emerging bistatic radar-based technique that utilizes the GNSS direct (transmitter-receiver) and reflected (transmitter-reflection point-receiver) signals to extract properties of the reflecting surface. This study explores the potential of airborne GNSS-R as a means to monitor sea state in coastal areas by using the Doppler spread and reflectivity as observables. The paper aims to derive a sea state factor from the reflected signal power and the Doppler shift distribution to analyze its correlation with wind speed and significant wave height data obtained from the ERA5 model. The experiment involved four flights conducted along the coast between Calais and Boulogne-sur-Mer, France, in July 2019. A GNSS software receiver processes the direct and reflected signals, tracking and re-tracking the reflected signals with the aid of a specular reflection model. The resulting in-phase and quadrature components are analyzed in the spectral domain every minute to estimate the power, the surface reflectivity, and the relative Doppler shift. The findings reveal that the sea state factor and Doppler spreading are sensitive to sea state conditions, correlated with the ERA5 parameters, and influenced by the elevation angle of GNSS satellites. At low elevations (E<10°), the sea state factor demonstrates an inverse relationship (anti-correlation) with the wind speed and significant wave height, while the Doppler distribution shows a correlation with these

1   German Aerospace Center (DLR), Alemania, e-mail: mario.moreno@dlr.de.
     ORCID: https://orcid.org/0009-0009-9124-8063

parameters. Both correlations decrease with increasing elevation angle. This research underscores the potential of airborne GNSS-R for monitoring sea state variability in coastal areas enhancing our understanding of the relationships between GNSS-R measurements and sea state parameters.

Abstract

El aumento del nivel del mar y la variabilidad del estado del mar, como resultado del cambio climático y el calentamiento global, son áreas de investigación críticas. Sin embargo, las técnicas actuales para observar y monitorear estos fenómenos tienen limitaciones en términos de resolución espacial y temporal, especialmente en zonas costeras. GNSS Reflectometría (GNSS-R) es una técnica emergente basada en radar biestático que utiliza señales GNSS directas (transmisor-receptor) y reflejadas (transmisor-punto de reflexión-receptor) para extraer propiedades de la superficie reflejante. Este estudio explora el potencial de la GNSS-R aérea como medio para monitorear el estado del mar en áreas costeras utilizando el efecto Doppler y la reflectividad como observables. El objetivo es calcular un factor de estado del mar (SSF) a partir de la potencia de la señal reflejada y analizar la distribución del desplazamiento Doppler para evaluar su correlación con la velocidad del viento y la altura significativa de las olas obtenidas del modelo ERA5. El experimento consistió en cuatro vuelos realizados entre Calais y Boulogne-sur-Mer (Francia) en Julio de 2019. Las señales se procesan mediante un receptor de software, rastreando las señales reflejadas asistido por un modelo de reflexión especular. Las señales resultantes se analizan en el dominio espectral cada minuto para estimar la reflectividad de la superficie y el desplazamiento Doppler relativo. Los resultados revelan que el SSF y la dispersión Doppler son sensibles a las condiciones del estado del mar, correlacionadas con los parámetros del modelo ERA5 e influenciadas por el ángulo de elevación de los satélites GNSS. A bajas elevaciones (E<10°), el factor de estado del mar muestra una relación inversa con la velocidad del viento y la altura de las olas, mientras que la distribución Doppler muestra una correlación positiva con estos parámetros. Ambas correlaciones disminuyen a medida que aumenta el ángulo de elevación.

Palabras claves: GNSS Reflectometría aerotransportada, estado del mar, Dispersión Doppler, Reflectividad, Cambio climático.

1. Introduction

Climate change is a prominent research topic across various scientific disciplines, attracting significant attention within the scientific community. Over the past few decades, numerous studies have been conducted to evaluate the potential risks and hazards associated with climate change and its implications for both humans and the environment. Coastal areas are marked

by dense population centers, extensive socio-economic activity, and essential infrastructure vital for supporting human livelihoods reliant on ocean resources (Vousdoukas *et al.*, 2018). These coastal regions are dynamic systems subject to a wide array of natural and human-induced influences. As a result, extensive research efforts have been dedicated to monitoring and analyzing the various factors that shape coastal zones and drive their ongoing transformations in response to changing climatic conditions. Figure 1 showcases the evolution of the beach in Chatham, MA, USA, spanning from 1985 to 2020. This visual representation highlights the continuous changes experienced by barrier beaches, primarily driven by rising sea levels, wave dynamics, currents, winds, tides, and human activities.
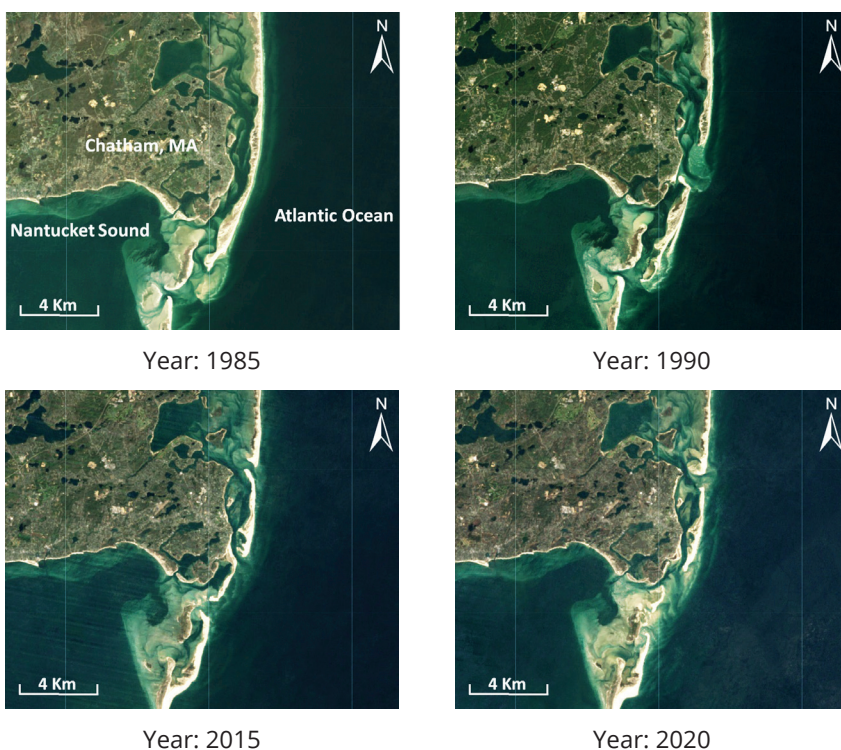

Year: 1985   Year: 1990

Year: 2015   Year: 2020

Figure 1.   Coastal barrier evolution in Chatham, MA, USA. Satellite images Landsat 5, 7 and 8

Sea level derivation is directly influenced by the heterogeneity of the sea surface and the presence of slopes, which are indicative of surface roughness. Surface roughness, in turn, can be interpreted as sea state, a significant factor of interest in coastal areas. Sea state refers to the characteristics of wind-generated waves, including their height, direction, and period (Webb, 2019). Previous

studies have highlighted the substantial impact of the wind-wave component on sea level variations along coastlines (Bengtsson *et al.*, 2006; Melet *et al.*, 2020). However, techniques for measuring sea level are more advanced compared to those for detecting winds and waves in coastal areas (Benveniste *et al.,* 2019).

In the early 1990s, it was introduced a multi-static radar concept that involved the utilization of Global Navigation Satellite Systems (GNSS) signals in an interferometric manner (Martín-Neira, 1993) . This approach entailed combining the direct GNSS signal with the signals reflected by the Earth's surface to retrieve the necessary parameters from the reflecting surface at the specular point (reflection point where the elevation angle of incident ray equals the angle of the reflected ray, see Figure 2). This technique, now known as GNSS Reflectometry (GNSS-R), has since been widely adopted and developed for altimetry, sea state estimations, sea ice presence, and soil moisture content or snow detection.
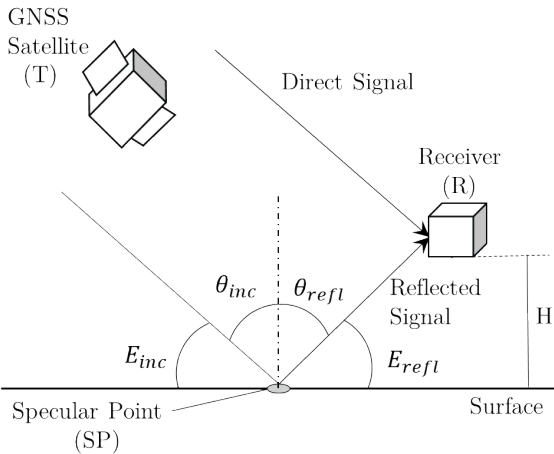

Figure 2. GNSS Reflectometry geometry representation. is the elevation angles and is the height between the reflecting surface and the GNSS-R platform.

For ocean applications, GNSS-R experiments have explored different setups and observables to retrieve sea level and sea state information. Alonso-Arroyo *et al.*, (2015) utilized a ground-based setup, employing the Interference Pattern Technique (IPT) to combine direct and reflected signals. They successfully determined Significant Wave Height (SWH) and Mean Sea Surface Level (MSSL) showing accuracies of 5.7 cm and 4.1 cm, respectively. In a similar setup, Geremia-Nievinski *et al.*, (2020) used the Signal to Noise radio as observable for coastal sea-level altimetry. Comparing with a co-located tide gauge, they obtained a RMSE smaller than 5 cm in sea level estimations. Promising results have also been obtained using airborne and spaceborne data. Semmling *et al.*, (2014) utilized a signal path model that leveraged the time difference between

the reflected and direct signals to estimate Sea Surface Topography (SST) using carrier phase data. Their investigation took place aboard a scientific aircraft positioned at an altitude of approximately 3500 meters, equipped with both an up-looking antenna and two portside-looking antennas. Impressively, they attained centimeter-level precision $\partial T_{std} < 10$ cm in SST estimation, encompassing elevation angles spanning from 11° to 33°. More recently, Cardellach *et al.*, (2020) utilized data from the spaceborne NASA Cyclone GNSS mission (CyGNSS) to retrieve sea surface altimetry under specific sea state conditions (wind speed below 6 m/s and significant wave height of 1.5 m). They implemented the Grazing Angles geometry condition (elevation angles up to 25°) and Carrier Phase-delay Altimetry (GA CaPA) technique, demonstrating precisions between 3-4 cm. These studies showcase the potential of GNSS-R for retrieving sea level and sea state information using various platforms and techniques.

The paper is organized as follows. Section 2, describes the experiment conducted in July 2019. It includes the study area description the used platform and antenna setup, data set collected, and the processing steps. Section 3 presents the results analyzing correlation between the sea state conditions and the sea state factor and Doppler spread estimations. Finally, Section 4 discusses the findings, limitations, and possible further applications based on the presented methodology.

A web-based geo-visualizer application has been developed as a supplementary tool to present the findings of this study. The interactive application, accessible at https://reflectometry-9098aae75e7f.herokuapp.com/ utilizes a map-based interface with user-friendly features. It enables users to apply filters to select the complete data set or specific subsets of data and visualize the results through plots. The application enhances the accessibility and usability of the results, providing an intuitive platform for interactive exploration and analysis.

2. Methodology

2.1 Experiment

In July 2019, an airborne GNSS-R measurements campaign was conducted along the Opal Coast in the North Sea, specifically between the cities of Calais and Boulogne-sur-Mer in France. Four flights were executed on the 12th, 15th, 17th, and 19th of July, following the same trajectory at a height of ~750 m. Each flight had a duration of approximately 1 hour, covering a total trajectory length of approximately 95 km over the ocean.

It should be noted that due to the limited availability of GPS satellites during the tracking phase along the west-to-east flight segment or insufficient reflection events over the sea surface, the focus of this study is on the North to South flight segment highlighted in orange in Figure 3.

Figure 3. Flight trajectory during measurements camping. The flight trajectory encompassed two distinct legs, with the first leg positioned at a distance of 700 m from the coastline, and the second leg situated at a distance of 2000 m.

Within the North to South flight segment, continuous reflection tracks were successfully retrieved from the selected satellites G1, G7, G8, G10, G11, G16, G18, and G30. Table 1 presents the sea state variations in the study area, characterized by the mean values of wind speed (WS), wind directions, and significant wave height (SWH). These parameters were derived from the ECMWF ERA5 model (Hersbach *et al.*, 2020) , which provides reliable data along the flight trajectory. Among the recorded dates, the lowest sea state conditions were observed on 2019/07/17.

Table 1. Sea state parameters from ERA5 Model

Date	Wind Speed [m/s]	Wind Direction [deg]	SWH [m]
2019/07/12	5.49	117	0.30
2019/07/15	4.29	67	0.58
2019/07/17	2.92	204	0.26
2019/07/19	6.50	240	0.55

The chosen platform is a gyrocopter presented in Figure 4. Gyrocopters are microlight aircraft that utilize autorotation for propulsion, enabling them to fly at low speeds with exceptional maneuverability. These aircraft demonstrate the capability to maintain stability and safety even in challenging weather conditions, including strong winds and turbulence.

Figure 4.   Gyrocopter used in the experiment. (1) GNSS - R antenna, (2) Extra GPS antenna + INS for flight control purposes.

For the GNSS-R measurements, a dual-polarization antenna was employed, featuring both right-handed and left-handed circular polarization positioned at the front of the aircraft. The antenna was tilted at an angle of approximately 43° relative to the zenith direction. Due to the absence of significant reflection responses from the left-hand polarized channel, the analysis in this experiment was limited to the signals received from the right-hand polarized channel. The antenna is connected to two receivers: a Syntony Echo-L receiver, which records the raw GPS L1 signals utilized for reflectometry analysis, and a Javad Delta GNSS receiver, which records RINEX messages for accurate trajectory solution during post-processing.

2.2 Data and Processing

The Syntony Echo-L receiver utilized to record GPS L1 signals, sampled the data at a frequency of 16.368 MHz. For each day, four raw datasets were acquired and they categorized as data level 0. Each dataset had a duration of approximately 18 minutes, corresponding to the north-to-south segment of the trajectory. The data level 1 corresponds to the complex direct and reflected signals at a frequency of 50 Hz after the tracking and re-tracking step. These signals are represented by the in-phase (I) and quadrature (Q) components, respectively. Data level 2 consisted of the estimation of the power peak for the Sea State Factor, relative Doppler shift, and Doppler Distribution of the residual reflected signal every 10 seconds. These estimates were derived from the Power Spectral Density and integrated over 1 minute.

The workflow of data processing in Figure 5 include the components and retrievals for each data level established. As mentioned earlier, this study focuses solely on processing the signals with right-handed circular polarization

(RHCP). However, the signals with left-handed circular polarization (LHCP) are recorded and archived for potential future investigations.
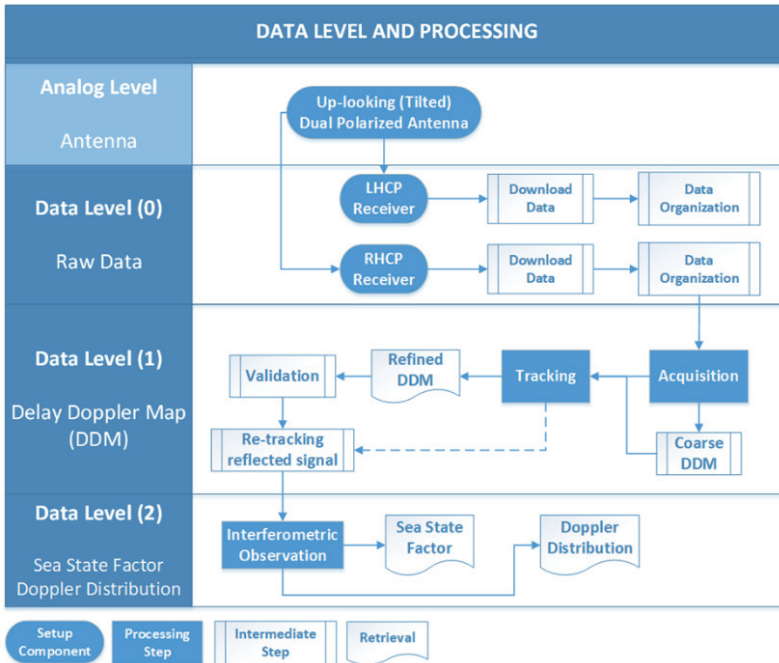

Figure 5.   Scheme of data levels and general processing steps. Only right-hand circular polarized signals are processed in this study.

2.2.1 Specular point and path difference model

A geometrical model is employed to determine specular point positions and path differences between the direct and reflected signals as presented in (Semmling *et al.*, 2012). The model incorporates Earth surface curvature and requires transmitter T_x and receiver R_x positions in an Earth-Centered Earth-Fixed (ECEF) frame. T_x is obtained from broadcasted ephemeris, while R_x is determined by postprocessing using nearby GNSS antennas of the French network (IGN, 2019) as reference stations. A spherical surface approximates the Earth's curvature, with an iterative process finding the best-fitting sphere satisfying the specular reflection condition. The final specular point (SP) undergoes geoid undulation correction using the EIGEN-6C2 model (Foerste *et al.*, 2013). The reflected path L^R is established between T_x, SP, and R_x, while the direct path L^D is modeled from T_x to R_x. The path difference $\Delta p(t)$, retrieved from $\Delta p = 2H \sin(E)$, represents the residual between the reflected and direct paths, influenced by changing satellite elevation and aircraft trajectory. Tropospheric and ionospheric delay corrections are excluded from the geometrical path model in this study. Figure 6 displays the

tracks of specular points obtained on July 17th for the eight analyzed satellites, PRN 1, 7, 8, 10, 11, 16, 18, and, 30.
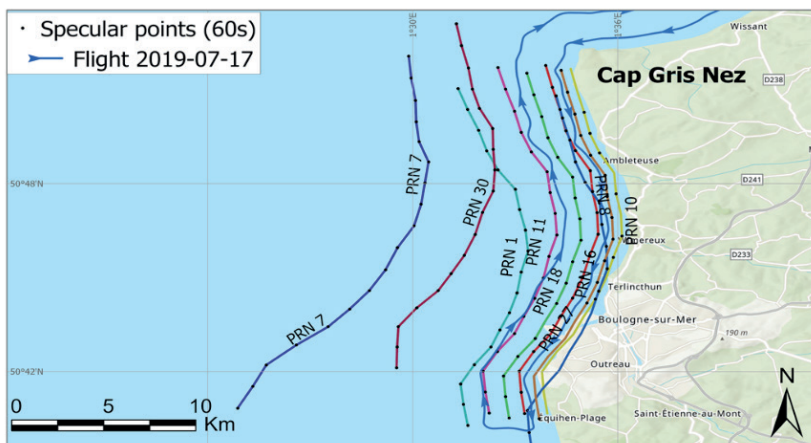

Figure 6. Specular point tracks on July 17th along the coast over sea surface every 60 seconds. Track colors denote the GNSS satellites analyzed: PRN 1, 7, 8, 10, 11, 16, 18, and, 30.

2.2.2 Signal tracking and re-tracking

The GNSS software receiver, based on the methodology described in (Kucwaj et al., 2017), is utilized to calculate the in-phase I_0^R and quadrature Q_0^R components of the reflected signal after the tracking stage. The starting point is the definition of the direct signal (S^D) and reflected signal (S^R) as follows:

$$S^D = A^D CA\big(t - \tau^D(t)\big) \sin\big(2\pi f^D t - \phi^D(t)\big) + \eta^D(t) \tag{1}$$

$$S^R = A^R CA\big(t - \tau^D(t) - \Delta_p(t)/c\big) \sin\big(2\pi f^D t - \phi^D(t) - \psi(t)\big) + \eta^R(t) \tag{2}$$

The direct signal amplitude is denoted as A^D, while the reflected signal amplitude is represented by A^R. CA corresponds to the code-division multiple access (CDMA) broadcasted by the GPS satellites. τ^D represents the code delay of the direct signal, and f^D and ϕ^D denote the frequency and phase delay, respectively. η^D and η^R represent zero-mean Gaussian noises. The path difference between the direct and reflected signals is given by Δ_p, with c representing the speed of light. The phase difference between the direct and reflected signals is denoted as ψ.

The tracking module utilizes a Delay Lock Loop DLL, a Phase Lock Loop (PLL), and a Frequency Lock Loop (FLL) with a 20 ms integration time to process the signals (Morton et al., 2020) robustness, and accuracy of performance. It begins with the objectives of signal tracking, followed by a conceptual description of a

closed-loop tracking system. A brief conventional treatment of code delay lock loop (DLL. A local replica of the direct signal is constructed based on the model in equation (1) represented by the in-phase ($p^{I,D}$) and quadrant $p^{Q,D}$ components. Using this replica, the reflected signal is demodulated, and its components I_0^R and Q_0^R are calculated using equations (3) and (4), respectively. These equations involve the measurement index (k) and the coherent integration time (T_c)of the direct signal tracking stage (20 ms)

$$I_0^R = \int_{k\,T_c}^{(k+1)T_c} S^R(t)p^{I,D}(t)dt \tag{3}$$

$$Q_0^R = \int_{k\,T_c}^{(k+1)T_c} S^R(t)p^{Q,D}(t)dt \tag{4}$$

Employing the geometrical path difference model, equations (5) and (6) provide the final expressions for (I_0^R) and (Q_0^R). In these equations, η_k^I and η_k^Q represent two independent zero-mean Gaussian noises, and   models the normalized correlation function of the CDMA code.

$$I_0^R = \frac{A^R}{2}\Lambda\left(-\Delta_{p,k}/c\right)\cos(-\psi_k) + \eta_k^I \tag{5}$$

$$Q_0^R = \frac{A^R}{2}\Lambda\left(-\Delta_{p,k}/c\right)\sin(-\psi_k) + \eta_k^Q \tag{6}$$

The removal of data bits from the direct signal is achieved by multiplying the (I_0^R) and (Q_0^R) components with the sign function of the in-phase component. Subsequently, a moving average filter is applied to extract the higher-frequency component of the reflected signal while removing the low-frequency contribution from the direct signal. The reorientation of the complex reflected filtered signal is given by $\gamma_c^R = I_c^R + iQ_c^R$. The phasor γ_c^R undergoes a retracking process using a module based on (Semmling, 2012), which corrects for variations in the transmitter and receiver trajectory, elevation angle, and reflecting surface height over time.

The reflected signal re-tracking process begins by modeling the phase difference   using the path difference model Δ_p. The phase difference ψ_P is obtained by taking the modulo of ($\frac{2\pi\Delta_p}{\lambda}, 2\pi$), where λ represents the wavelength of the GPS L1 signal (~0.1904 m). This phase difference is used to construct the phasor representation γ_p, given by $exp\left(-i\psi_p\right)$.

Finally, the re-tracked reflected signal, denoted as the residual phasor γ^R, is obtained by multiplying the phasor representation γ_c^R with the complex conjugate of the modeled phasor γ_p^*. The resulting γ^R is represented as $I^R + iQ^R$.

2.2.3. Reflectivity

In addition to analyzing the signal amplitude in the time domain, the Power Spectral Density (PSD) is employed to examine the power distribution of the residual re-tracked signal in the Doppler domain. Following the approach described in (Semmling *et al.*, 2013), the PSD is defined as the Fourier amplitude of the reflected signal, represented as $|\mathfrak{F}\{\gamma^R\}(f)|$, where $\mathfrak{F}\{\}$ denotes the Fourier Transformation. The computation of the Power Spectral Density is performed at intervals of 10 seconds for each satellite, allowing for an analysis of the power distribution across different Doppler shifts.

In the PSD representation, sharper and distinct peaks are observed in cases of low sea state (2019/07/17). The broadening of the spectrum is also influenced by the roughness of the sea surface, as evidenced by the wider spread observed on 2019/07/12 (during higher sea state) compared to 2019/07/17. This suggests that the presence of multiple scatters in different directions, caused by increased surface roughness, contributes to the incoherent reflection process. Figure 7 illustrates the PSD comparison of the reflected signal for PRN 30 on different days, representing both low and high sea state conditions.
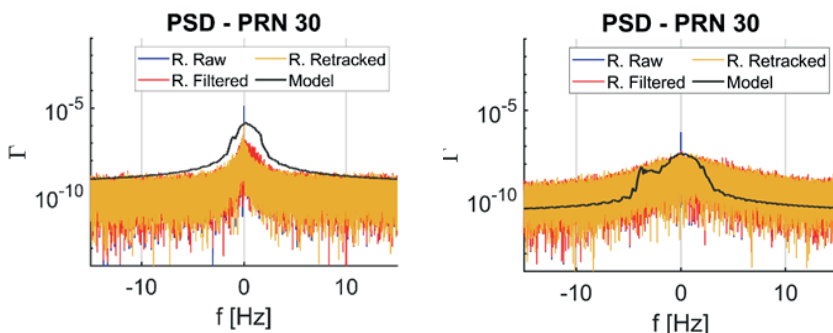

Figure 7. PSD for PRN satellite 30 on July 17th (left) at lower sea state and on July 12th (right) higher sea state. Elevation angle .

The reflectivity, which quantifies the power ratio between the reflected signal and the direct signal, can be computed using the spectral approach. By analyzing the power peaks of the raw complex direct signal $(max\ (\Gamma^D))$ and the retracked reflected signal $(max\ (\Gamma^R))$, the observed reflectivity (R_o) in decibels [dB] can be determined in equation (7), evaluated over a specific time period (T).

$$R_o = 10 \cdot \log_{10} \left[\frac{\max(\Gamma^R)}{\max(\Gamma^D)}\right]_{T_a}^{T_b}$$

Figure 8 displays the plot of reflectivity against the elevation angle. The comparison is made between two dates: 2019/07/17 (dots) and 2019/07/19 (stars), representing low and high sea state conditions, with wind speeds of approximately 2.92 m/s (SWH: 0.26 m) and 6.5 m/s (SWH: 0.55 m) respectively. The black line represents the modeled ocean surface reflectivity. On 2019/07/17 (low sea state), satellites at low and mid-elevation angles closely match the reflectivity model, while high-elevation satellites exceed the modeled values, indicating non-specular reflection. Additionally, on 2019/07/19 (roughest sea surface), the reflectivity is significantly lower for all events.
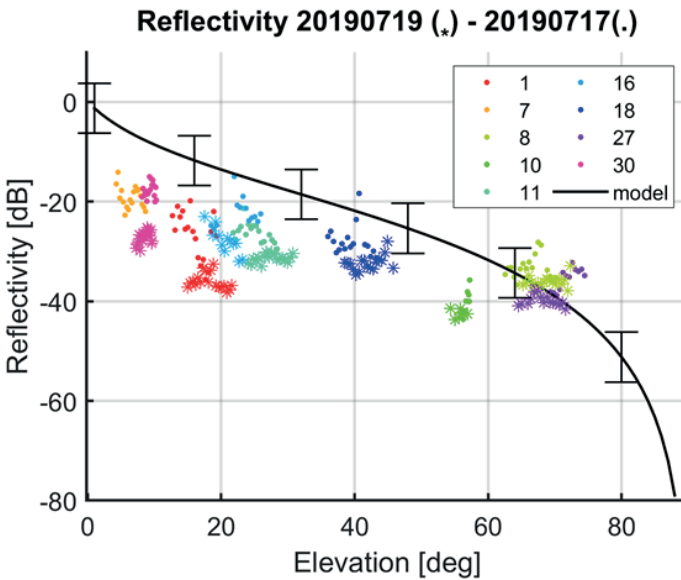

Figure 8. Reflectivity against elevation angles on July 19th (stars) and July 17th (dots). Both days maintain a similar reflectivity-elevation relation with lower values on 19th due to rougher surface.

The residual obtained by subtracting the observer reflectivity R_o from the modeled reflectivity R_m is referred to as the sea state factor ($SSF = R_o - R_m$). This parameter is utilized to assess the correlation between the reflectivity derived from power observations and the accompanying sea state parameters obtained from the ERA5 model. Results are presented in section 3.1.

2.2.4 Doppler Spreading

The analysis of Doppler frequency shift in GNSS-R has proven useful for ocean altimetry and surface ocean roughness estimation, as demonstrated in previous studies (Semmling et al., 2013; Semmling, 2012)and thus Doppler residuals are retrieved. This correction reduces the width of the spectral reflection peak from

3 mHz to less than 10 mHz. Doppler residuals are sensitive to surface height. Lake level is estimated inversely for the residuals at different trial heights. A case study of reflection events is presented. Lake level is estimated using data from antennas with right-handed and left-handed circular polarization. Reference level is determined from tide gauge data for stations around the lake. Mean deviation of estimates from reference level is 50 cm. Doppler shifts of different model corrections are compared. The altimetric correction is the most important, with mean Doppler shifts between 316 and 560 mHz. Mean Doppler shifts are much smaller for baseline correction (less than 0.2 mHz. The PSD analysis within a specific time interval enables the identification of the relative Doppler effect by locating the maximum peak in the frequency domain (x-axis). The displacement from the relative frequency indicates the magnitude of the Doppler shift. Figure 9 shows that during a low sea state (2019/07/17) at low elevation angles, the Doppler shift remains close to zero with minimal variations. Conversely, a higher sea state results in significantly increased variations which are also influenced by the elevation angles.
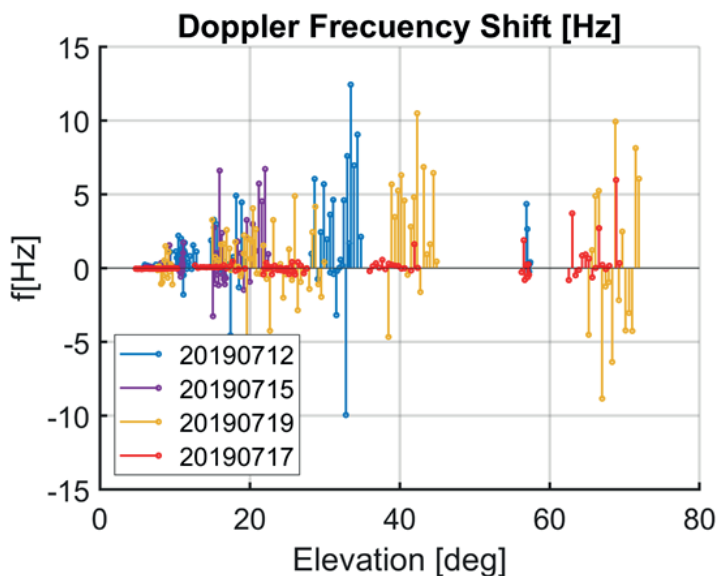

Figure 9. Doppler Frequency shift and elevation angles grouped by date. Doppler distribution has a dependency on elevation angles and sea surface roughness

The Doppler spread, which characterizes the variation of Doppler shifts, is influenced by the random behavior of ocean waves (Elfouhaily et al., 2002). In order to assess the distribution of Doppler shifts related to the sea state in this study, the standard deviation of Doppler shifts is calculated over 120-second

intervals. Results of the Doppler spreading and correlation with sea state conditions are presented in section 3.2.

3. Results

The results presented in this section provide insights into the behavior of events across various ranges of elevation angles. By categorizing the events into different groups, namely low (E < 10°), mid (10° < E < 30°), and high (E > 30°), we can examine how the observed phenomena vary with respect to changes in the elevation angle. This categorization allows for a more comprehensive analysis of the data and helps to identify distinct patterns and trends within each group.

The wind speed and significant wave height data obtained from the ERA5 model are stored in raster format. The spatial resolution of the WS raster is 18 km and 25 km for the SWH, respectively. In order to extract the values at the positions corresponding to the specular points, a geo-interpolation technique is applied. This interpolation method considers both the pixel values and the localization of the points, resulting in a smoother retrieval of the respective parameters.

3.1 Sea state factor (SSF) and sea state

SSF values above zero indicate the dominance of the incoherent component in the reflection process, deviating from the specular reflection model. These events mainly occur at high elevation angles. The sea state factor shows a decreasing trend as sea state conditions vary across different data collection dates. Figure 10 presents the sea state factor results grouped by date, where the SSF values on July 17th are notably the highest, aligning with the reflectivity findings.

Specular reflection occurs primarily at low elevation angles and on surfaces with low roughness. Wind speed is directly proportional to wave generation, and higher wind speeds correspond to increased sea surface roughness. This relationship is supported by Figure 11 (left), which shows that the power loss in the reflected signal, represented by the SSF, aligns with the wind speed retrieved from the ERA5 model, indicating an increase in sea state. At the lowest sea state, the SSF values are concentrated around -10 dB, while at higher sea states, the values are more spread out and can decay to -30 dB. Similarly, the SSF values exhibit a similar trend with SWH (Figure 11 right) indicating a higher loss of reflected signal power as SWH increases. However, the effect is less pronounced due to the larger spatial resolution of the SWH (25 km), which produces interpolated values being similar at adjacent locations.
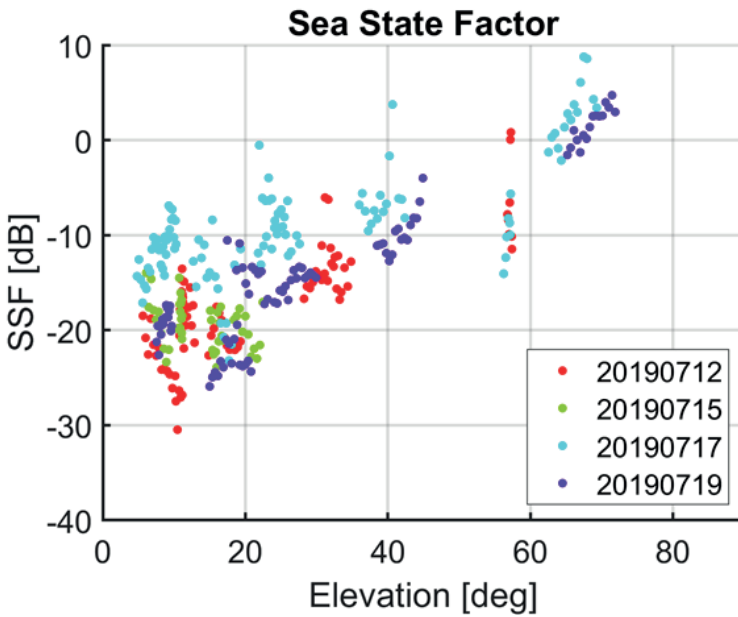
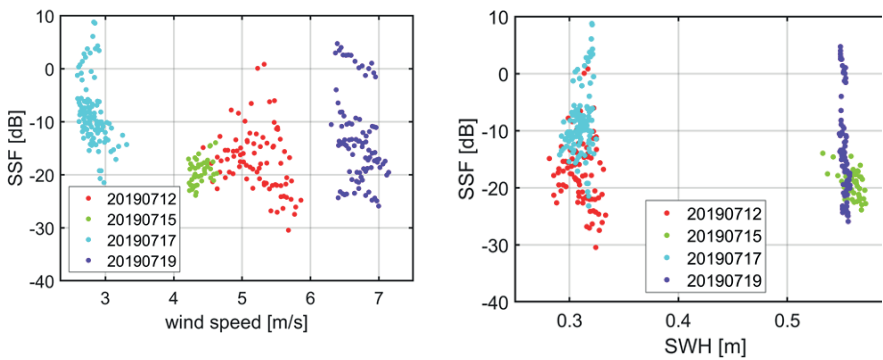**Figure 10.** Sea state factor at different elevation angle events grouped by date of data collection.

Figure 11. A color-coded plot of the sea state factor (SSF) and wind speed measurements by date on the left side. SSF and SWH by date on the right side.

Figure 12 presents a bivariate map showing the variability of the sea state factor (SSF) in relation to changes in elevation angle at the specular point locations for each satellite. The map uses a color scale, with pink representing SSF and blue representing elevation. By combining both color scales, the resulting map displays high elevation values with high (negative) SSF as dark blue, while low elevation values with low (negative) SSF are represented by light pink.
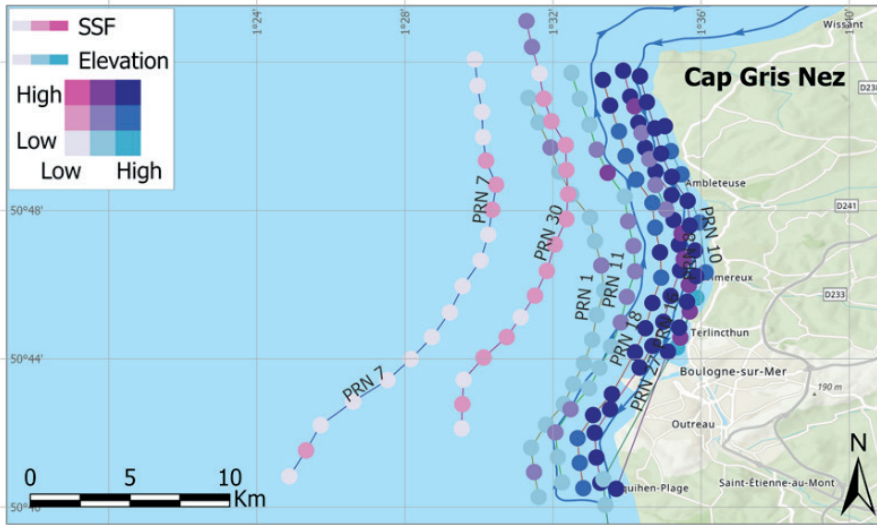
Figure 12. Map of SSF variability with respect to elevation angle change. At high elevation angles, are found highest (negative) sea state factor.

Pearson correlation coefficients between the sea state factor (SSF) and the sea state parameter for different elevation angle groups is presented in Table 2.

The sea state factor exhibits a strong negative correlation with wind speed and a moderate negative correlation with significant wave height (SWH). This negative correlation aligns with the expected behavior, where higher sea states lead to a decrease in the power of the reflected and re-tracked signal, and vice versa. Additionally, a noticeable correlation pattern is observed with respect to elevation angles. Events at low elevation angles demonstrate the highest negative correlation, while the correlation decreases as elevation angles increase. Notably, events in the high elevation range do not exhibit a significant correlation with the sea state factor.

Table 2. Correlations of SSF with wind speed and SWH

Date	SSF	SSF	SSF
Wind Speed	-0.7643	-0.4639	-0.1221
SWH	-0.5066	-0.3775	-0.0007

3.2 Doppler Spreading and sea state

The findings highlight the relationship between the Doppler shift and the combined influence of sea state and elevation angle. The observed mean (Table 3) the Doppler shift on July 17 were notably lower than those recorded on the other dates. This suggests that the sea state and elevation angle conditions

during that period resulted in reduced variations in the Doppler shift. In contrast, higher sea state conditions, combined with elevated elevation angles, led to an increase in both the mean Doppler shift. These results indicate the significant impact of sea state and elevation angle on the Doppler shift measurements, emphasizing their role in the characterization of ocean surface dynamics.

Table 3. Mean values of Doppler shift at different elevation angles

Date	Doppler Mean	Doppler Mean	Doppler Mean
2019/07/12	0.2188	0.9566	1.8949
2019/07/15	0.2459	0.8839	~
2019/07/17	-0.0301	-0.0058	0.4509
2019/07/19	-0.0649	0.5722	1.7262

Figure 12 depicts the bivariate map of Doppler shift variability at various elevation angles along the segment analysis from Cap Gris Nez. Similar to the bivariate map of SFF and elevation angles, a color scale is provided for each variable, with pink representing Doppler frequency shift and blue representing elevation angles. Dark blue corresponds to high elevation values with high Doppler frequency shift, while light pink represents low elevation values with low Doppler frequency shifts. This visualization enables the examination of the spatial distribution of Doppler shift variations in relation to elevation angles along the analyzed segment.
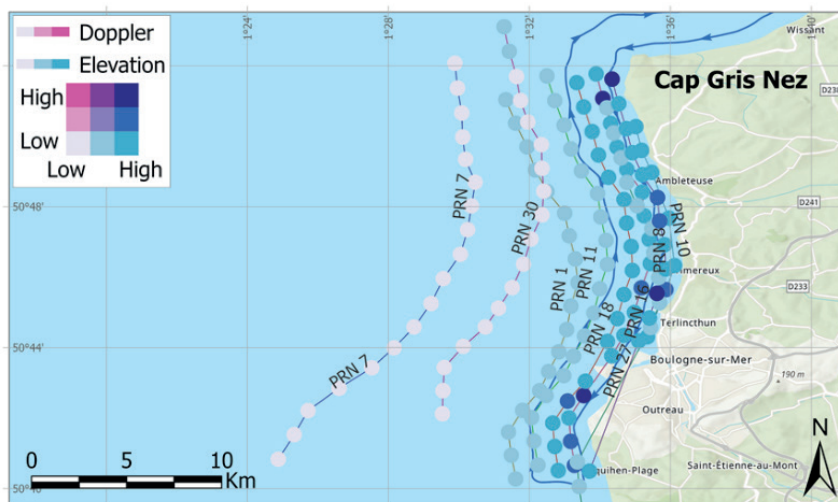

Figure 13. Map of Doppler shift with respect to elevation angle change.

Pearson correlation coefficients between the Doppler spreading and the sea state parameters for different elevation angle groups is presented in Table 4.

The standard deviation of the Doppler shift demonstrates a strong positive Pearson correlation with wind speed and SWH. This positive correlation indicates that increasing sea state conditions lead to higher variations in the Doppler shift, as depicted in Figure 9. Furthermore, the correlation between the Doppler spreading and sea state parameters is influenced by the transmitter elevation angles. The strongest correlation is observed at low elevation angles, while it significantly decreases for events with elevations above 10°. In the mid and high elevation ranges, events exhibit a moderate correlation with sea state parameters, with no significant changes in correlation within these elevation ranges. This implies that at higher elevation angles, the relationship between the Doppler spreading and the sea state parameters becomes weaker, indicating a lesser impact of sea state conditions on the observed Doppler shift variability.

Table 4. Correlations of SSF with wind speed and SWH

Parameter	Doppler Spread $E < 10^o$	Doppler Spread $10^o < E < 30^o$	Doppler Spread $E > 30^o$
Wind Speed	0.9421	0.6395	0.6080
SWH	0.8530	0.6061	0.5691

4. Discussion and conclusions

Coastal areas, vulnerable to climate change-induced sea level rise and sea state variability, can be monitored using GNSS reflectometry. This study introduces a novel approach to examine sea state parameters in these zones by analyzing GNSS satellite signals. Previous studies have demonstrated the potential of GNSS reflectometry in ground-based and space-borne experiments for sea state retrievals. This experiment expands on that research by investigating the sensitivity of the reflected signal to sea state changes using low-altitude airborne measurements, aiming to estimate wind speed and significant wave height in future work.

The results demonstrate a correlation between the reflectometry retrievals and sea state parameters from ERA5, indicating the feasibility of retrieving sea state (surface roughness) from airborne GNSS-R measurements in coastal zones. The sea state factor exhibits a high and moderate degree of anti-correlation with wind speed and significant wave height (SWH), respectively, depending on the elevation angle. Strong anti-correlations are observed at low elevation angles (E<10°), while the correlation weakens at higher elevations, aligning with the specular reflection model.

The Doppler spread, a measure of the variation in Doppler frequency shift, is highly responsive to changes in sea surface roughness. It demonstrates lower values during periods of calm sea states and higher values during times of more turbulent sea conditions, especially at low elevations. The Doppler spreading

exhibits a significant correlation with wind speed and significant wave height, particularly noticeable at low elevation angles. However, as the elevation angle increases, the correlation gradually diminishes.

In addition, in situ observations are essential for cross-validating the results obtained from remote sensing technique GNSS-R. These ground-based measurements provide a crucial reference point to assess the accuracy and reliability of the sea state parameters correlation.

The experimental setup, including the up-looking antenna and receiver configuration, performed well for data collection. The analysis focused on signals from the RHCP receiver, with future work considering LHCP signals and the correction of antenna gain pattern. Additionally, alternative antenna setups and configurations, such as side-looking or down-looking antennas as presented in (Issa *et al.*, 2021), have demonstrated significant improvements in the final results. This highlights the importance of exploring different antenna arrangements to optimize signal reception and enhance the accuracy of sea state parameter retrievals in GNSS-R studies.

The selected gyrocopter platform proved to be suitable, facilitating stable flights aligned with the flight plan. Signal losses were observed in sections with significant changes in the gyrocopter's sight direction, attributed to antenna orientation and aircraft frame obstruction. Different antenna setups and flight trajectories can be considered for future experiments to optimize signal collection.

Drawing from the findings, there exists a promising opportunity to formulate a methodology for precise characterization of the sea surface through GNSS-R airborne measurements. However, factors such as precise receiver positioning, analysis of height fluctuations and aircraft attitude, and consideration of tropospheric and ionospheric corrections are crucial. Scaling the methodology to space-borne measurements requires further research. Additionally, investigating the correlation between wind direction and Doppler retrievals from GNSS-R and developing models for deriving wind direction from airborne data would be valuable areas of future study.

Bibliography

Alonso-Arroyo, A., Camps, A., Park, H., Pascual, D., Onrubia, R. & Martin, F. (2015). Retrieval of Significant Wave Height and Mean Sea Surface Level Using the GNSS-R Interference Pattern Technique: Results From a Three-Month Field Campaign. *IEEE Transactions on Geoscience and Remote Sensing*, 53 (6), 3198-3209. DOI: https://doi.org/10.1109/TGRS.2014.2371540

Bengtsson, L., Hodges, K. I. & Roeckner, E. (2006). Storm Tracks and Climate Change. *Journal of Climate*, 19 (15), 3518–3543. https://doi.org/10.1175/JCLI3815.1

Benveniste, J., Cazenave, A., Vignudelli, S., Fenoglio-Marc, L., Shah, R., Almar, R., Andersen, O., Birol, F., Bonnefond, P., Bouffard, J., Calafat, F., Cardellach, E., Cipollini, P., Le Cozannet, G., Dufau, C., Fernandes, M. J., Frappart, F., Garrison, J., Gommenginger, C., Wöppelmann, G. (2019). Requirements for a Coastal Hazards Observing System. *Frontiers in Marine Science*, 6. DOI: https://doi.org/10.3389/fmars.2019.00348

Cardellach, E., Li, W., Rius, A., Semmling, M., Wickert, J., Zus, F., Ruf, C. S. & Buontempo, C. (2020). First Precise Spaceborne Sea Surface Altimetry With GNSS Reflected Signals. *IEEE Journal of Selected Topics in Applied Earth Observations and Remote Sensing*, 13, 102-112. DOI: https://doi.org/10.1109/JSTARS.2019.2952694

Elfouhaily, T., Thompson, D. R., & Linstrom, L. (2002). Delay-Doppler analysis of bistatically reflected signals from the ocean surface: Theory and application. *IEEE Transactions on Geoscience and Remote Sensing*, 40 (3), 560-573. DOI: https://doi.org/10.1109/TGRS.2002.1000316

Foerste, C., Bruinsma, S., Flechtner, F., Marty, J.-C., Dahle, C., Abrykosov, O., Lemoine, J.-M., Neumayer, H., Barthelmes, F., Biancale, R. & König, R. (2013). EIGEN-6C2—A new combined global gravity field model including GOCE data up to degree and order 1949 of GFZ Potsdam and GRGS Toulouse. *Geophys. Res. Abstr. EGU Gen. Assembl.*, 15, 4077.

Geremia-Nievinski, F., Hobiger, T., Haas, R., Liu, W., Strandberg, J., Tabibi, S., Vey, S., Wickert, J. & Williams, S. (2020). SNR-based GNSS reflectometry for coastal sea-level altimetry: Results from the first IAG inter-comparison campaign. *Journal of Geodesy*, 94 (8), 70. DOI: https://doi.org/10.1007/s00190-020-01387-3

Hersbach, H., Bell, B., Berrisford, P., Hirahara, S., Horányi, A., Muñoz-Sabater, J., Nicolas, J., Peubey, C., Radu, R., Schepers, D., Simmons, A., Soci, C., Abdalla, S., Abellan, X., Balsamo, G., Bechtold, P., Biavati, G., Bidlot, J., Bonavita, M., ... Thépaut, J. (2020). The ERA5 global reanalysis. *Quarterly Journal of the Royal Meteorological Society*, 146 (730), 1999-2049. DOI: https://doi.org/10.1002/qj.3803

IGN (2019). GNSS Permanent Network | RGP. https://rgp.ign.fr/

Issa, H., Stienne, G., Reboul, S., Raad, M. & Faour, G. (2021). Airborne GNSS Reflectometry for Water Body Detection. *Remote Sensing*, 14, 163. DOI: https://doi.org/10.3390/rs14010163

Kucwaj, J. C., Reboul, S., Stienne, G., Choquel, J. B. & Benjelloun, M. (2017). Circular Regression Applied to GNSS-R Phase Altimetry. *Remote Sensing*, 9 (7), 651. DOI: https://doi.org/10.3390/rs9070651

Martín-Neira, M. (1993). A Passive Reflectometry and Interferometry System (PARIS): Application to ocean altimetry. *ESA Journal*, 17, 331-355.

Melet, A., Teatini, P., Le Cozannet, G., Jamet, C., Conversi, A., Benveniste, J., & Almar, R. (2020). Earth Observations for Monitoring Marine Coastal Hazards and Their Drivers. *Surveys in Geophysics*, 41 (6), 1489-1534. DOI: https://doi.org/10.1007/s10712-020-09594-5

Morton, Y. T. J., Yang, R. & Breitsch, B. (2020). GNSS Receiver Signal Tracking. In *Position, Navigation, and Timing Technologies in the 21st Century* (pp. 339–375). John Wiley & Sons, Ltd. DOI: https://doi.org/10.1002/9781119458449.ch15

Semmling, A. M., Schmidt, T., Wickert, J., Schön, S., Fabra, F., Cardellach, E. & Rius, A. (2012). On the retrieval of the specular reflection in GNSS carrier observations for ocean altimetry. *Radio Science*, 47 (6). DOI: https://doi.org/10.1029/2012RS005007

Semmling, A., Wickert, J., Schön, S., Stosius, R., Markgraf, M., Gerber, T., Ge, M. & Beyerle, G. (2013). A zeppelin experiment to study airborne altimetry using specular Global Navigation Satellite System reflections. *Radio Science*, 48, 427-440. DOI: https://doi.org/10.1002/rds.20049

Semmling, M. (2012). *Altimetric monitoring of Disko Bay using interferometric GNSS observations on L1 and L2* (pp. 1–136) [Deutsches GeoForschungsZentrum GFZ Potsdam]. DOI: https://doi.org/10.2312/GFZ.b103-12049

Semmling, M., Beyerle, G., Beckheinrich, J., Ge, M. & Wickert, J. (2014). Airborne GNSS eflectometry using crossover reference points for carrier phase altimetry. *2014 IEEE Geoscience and Remote Sensing Symposium*, 3786–3789.
DOI: https://doi.org/10.1109/IGARSS.2014.6947308

Vousdoukas, M. I., Mentaschi, L., Voukouvalas, E., Verlaan, M., Jevrejeva, S., Jackson, L. P., & Feyen, L. (2018). Global probabilistic projections of extreme sea levels show intensification of coastal flood hazard. *Nature Communications*, 9 (1), Article 1.
DOI: https://doi.org/10.1038/s41467-018-04692-w

Webb, P. (2019). I*ntroduction to Oceanography. Rebus Community.*
https://rwu.pressbooks.pub/webboceanography/